universe

MDPI

Article

Segmented Polar Motion Prediction Based on Varying Effective Angular Momentum Forecast Horizons

Yangyang Cui [1,2,3], Xishun Li [1,3], Yuanwei Wu [1,2,3,*], Haihua Qiao [1,3], Dang Yao [1,3], Zewen Zhang [1,2,3], Zhizhuo Zhang [1,2,3] and Xuhai Yang [1,2,3]

[1] National Time Service Center, Chinese Academy of Sciences, Xi'an 710600, China; cuiyangyang@ntsc.ac.cn (Y.C.); lixishun@ntsc.ac.cn (X.L.); qiaohh@ntsc.ac.cn (H.Q.); yaodang@ntsc.ac.cn (D.Y.); zhangzewen@ntsc.ac.cn (Z.Z.); zhangzhizhuo@ntsc.ac.cn (Z.Z.); yyang@ntsc.ac.cn (X.Y.)
[2] School of Astronomy and Space Science, University of Chinese Academy of Sciences, Beijing 100049, China
[3] Key Laboratory of Time Reference and Applications, Chinese Academy of Sciences, Xi'an 710600, China
* Correspondence: yuanwei.wu@ntsc.ac.cn

Abstract

Polar motion (PM), a key component of Earth orientation parameters (EOPs), is essential for high-precision satellite orbit determination and deep-space navigation. However, delays in data acquisition and processing limit its availability for real-time applications, necessitating the development of prediction models based on historical observations. Common approaches include least squares extrapolation (LS), autoregressive (AR) models, and their combination (LS + AR), often enhanced by effective angular momentum (EAM) from Earth's fluid components. This study examines an EAM + LS + AR method for PM prediction, systematically evaluating how different EAM forecast horizons (1–10 days) affect 90-day prediction accuracy for both PM X and Y components. A segmented optimization strategy is proposed and validated against International Earth Rotation and Reference Systems Service (IERS) official predictions using the IERS EOP 14 C04 product. Key findings include: (a) Adjusting the EAM horizon substantially reduces prediction errors. Segmented prediction improves PM X accuracy by 20–30% (1–60 days) and 10–20% (61–90 days) relative to IERS rapid products, while PM Y short-term accuracy improves by 20–40% (1–15 days). (b) The influence of EAM horizon on long-term PM Y prediction gradually weakens, with errors converging to approximately 8 mas by day 90. (c) For 1–10-day forecasts, optimal horizons follow a systematic pattern: day m predictions achieve the highest accuracy using an (m−1)-day EAM horizon, while a 10-day horizon is optimal for long-term forecasts. (d) The proposed method shows clear advantages over IERS forecasts, with 83.5% of PM X predictions (1–90 days) and 50.78% of PM Y predictions (1–15 days), outperforming IERS daily products during the 2024 test period.

Keywords: PM; forecast accuracy optimization; EAM; LS; AR

Check for updates

Academic Editors: Jiacheng Liu and Shilong Liao

Received: 24 April 2026
Revised: 6 June 2026
Accepted: 11 June 2026
Published: 12 June 2026
Corrected: 10 August 2026

Copyright: © 2026 by the authors. Licensee MDPI, Basel, Switzerland. This article is an open access article distributed under the terms and conditions of the Creative Commons Attribution (CC BY) license.

1. Introduction

Earth orientation parameters (EOPs)—which include length of day (LOD), Universal Time (UT1), polar motion (PM), precession, and nutation—capture the variations in Earth's rotational rate [1,2]. Real-time access to accurate EOP is crucial for satellite navigation, deep-space exploration, and ground-based astronomy. Among these parameters, PM describes the instantaneous displacement of Earth's rotation axis relative to the crust [3] and plays a key role in transforming between terrestrial and celestial reference frames. In practice, EOP

solutions derived from modern space-geodetic techniques such as Very Long Baseline Interferometry (VLBI), Global Navigation Satellite System (GNSS), and Satellite Laser Ranging (SLR) are typically available with latencies ranging from hours to days, which fall short of real-time operational demands [4,5]. The International Earth Rotation and Reference Systems Service (IERS), the primary authority providing Earth Rotation Parameters (ERP), releases its final PM product with a delay of about 30 days; even its rapid product is delayed by roughly one day [6–8]. Given this latency, forecasting PM for the coming days becomes essential for systems like BeiDou—without such forecasts [9], orbit determination errors can reach kilometer-level magnitudes. Therefore, advancing PM forecasting techniques to bridge the observation gap holds substantial practical value [10,11].

A wide range of EOP prediction models has been developed to enhance forecasting accuracy [12], encompassing linear, nonlinear, and hybrid approaches. Linear extrapolation is frequently implemented using a polynomial least squares (LS) model fitted to historical time series [13], which effectively captures both secular trends and the primary periodic components of PM [14–16]. Autoregressive (AR) models are also employed to leverage serial correlation within PM series, thereby improving short- to medium-term prediction performance. Time series models such as ARMA (Autoregressive Moving Average) and ARIMA (Autoregressive Integrated Moving Average) have been applied separately to the X and Y components of PM and have proven effective for short-term forecasting. On the nonlinear side, artificial neural networks [17], grey models, and wavelet-based approaches have been explored and have yielded promising outcomes [18,19]. Hybrid models seek to combine the strengths of multiple methods to achieve superior skill; among these, the LS + AR combination is widely regarded as one of the most effective schemes for PM prediction. In recent years, hybrid approaches incorporating physical excitation data have attracted growing interest. For example, the German Research Centre for Geosciences (GFZ) proposed integrating forecasts of effective angular momentum (EAM) derived from Earth's fluid components with the LS + AR method, significantly improving short-term EOP prediction accuracy [20]. Li et al. further advanced this idea by denoising EAM data to reduce the impact of anomalous signals in raw atmospheric angular momentum records [6,8,12]. Moreover, recent studies have integrated deep learning into traditional frameworks—such as coupling LS + AR with the Informer sequence network—to enhance medium- to long-term PM prediction. Different methods exhibit distinct strengths: incorporating atmospheric angular momentum (AAM) generally yields higher accuracy for short-term forecasts, whereas LS + AR-type models tend to perform better on seasonal and longer timescales [21]. During the 1st EOP Prediction Comparison Campaign (EOP PCC) conducted from 2005 to 2008, major prediction approaches were systematically evaluated [20,22,23]. More recently, the 2nd EOP PCC (2021–2022) indicated that LS + AR schemes incorporating EAM observations and forecasts perform particularly well for short-term UT1–UTC and LOD predictions [23,24]. These findings underscore that assimilating angular-momentum information from atmospheric, oceanic, and other fluid sources has become a key strategy for improving EOP forecast skill.

PM variability arises from two primary mechanisms: (i) intrinsic Earth dynamics, such as the free nutation (Chandler wobble, with a period of approximately 433 days) and the annual term [25–27], and (ii) external excitation resulting from angular-momentum exchange among the atmosphere, oceans, and continental hydrosphere [28–30]. This external influence is typically characterized by EAM functions, which include contributions from AAM, oceanic angular momentum (OAM), hydrological angular momentum (HAM), and sea-level-related effects (SLAMs). Mass redistribution and motion changes within these fluid components transfer angular momentum to the solid Earth through coupled interactions, thereby inducing variations in both the Earth's rotation rate and PM [28,31,32].

In addition to fluid excitation from the atmosphere, oceans, and hydrosphere, mass redistribution within the solid Earth can also perturb Earth's rotation and polar motion. A typical example is the 2004 Sumatra earthquake, for which Sabadini et al. investigated coseismic changes in Earth's rotation and showed that earthquake-induced deformation, topographic changes, and the compressibility of the Earth can influence rotational quantities [33]. As a result, incorporating EAM forecast data into PM prediction models is expected to enhance the representation of high-frequency signals. In most earlier applications, EAM forecasts were used with a fixed lead-time window (e.g., the 6-day forecasts traditionally provided by GFZ), without explicit examination of how the forecast horizon itself influences prediction performance. Recently, Li et al. explored variable EAM horizons for UT1 and LOD prediction and introduced a segmented forecasting framework, wherein shorter EAM horizons are applied for short-term predictions and longer horizons for medium- to long-term predictions, allowing for the selection of an optimal forecast window [12]. This approach led to substantial improvements in UT1–UTC prediction; compared to the conventional fixed 6-day EAM setting, the average accuracy of 90-day UT1 forecasts improved by more than 20% [12]. However, a comparable systematic investigation for PM prediction remains absent. Moreover, their study did not quantify in detail the specific impacts of different EAM forecast horizons on PM prediction accuracy. Therefore, understanding how to effectively utilize EAM forecasts with varying horizons in PM prediction is essential for further enhancing forecast performance [34–36].

In this study, we conduct a detailed investigation of the EAM + LS + AR approach for PM forecasting. The PM X and Y component time series for the entire year of 2024 are employed as the test dataset. Under conditions without EAM denoising and without considering X/Y coupling, 90-day PM forecasts are generated using a daily rolling strategy. For each prediction run, EAM forecast data with horizons varying from 1 to 10 days are incorporated into the LS + AR model, producing ten distinct sets of forecasts. This experimental design allows for a systematic evaluation of how the EAM forecast horizon affects PM prediction accuracy. Additionally, the resulting forecasts are compared with official IERS predictions to assess the effectiveness and advantages of the proposed method. Based on these analyses, we develop and present a segmented PM prediction strategy that adapts according to different EAM forecast horizons.

Previous EAM-assisted LS + AR studies mainly adopted a fixed EAM forecast window or focused on UT1–UTC and LOD prediction. In contrast, the present study systematically quantifies how EAM forecast horizons from 1 to 10 days affect 90-day PM X and PM Y prediction accuracy. The main contribution of this work is therefore not to replace the LS + AR prediction framework, but to optimize the physical excitation input window used in PM prediction and to develop a lead-time-dependent segmented EAM horizon strategy.

The remainder of this paper is organized as follows: Section 2 describes the data sources and the forecasting framework employed. Section 3 analyzes the impact of different EAM forecast horizons on prediction accuracy. Section 4 presents a comparative evaluation against IERS forecasts, followed by a discussion to determine the optimal EAM prediction horizon for extreme X/Y displacement predictions. Section 5 concludes the study.

2. Data and Methods

2.1. EAM and the Liouville Equations

In this study, the IERS EOP products are adopted as the reference ("truth") for evaluating PM predictions [3]. To maintain practical relevance for forecasting applications, we use the daily mean PM X(x_p) and Y(y_p) series from the IERS rapid product set—specifically, the 14 C04 solution under the IAU2000A conventions—covering the period from 1 January 2020 to 28 December 2024. Data from 2020 to 2023 are used for model development and

parameter estimation, while the full year 2024 is reserved for rolling forecast experiments and accuracy assessment.

EAM data represent the angular-momentum contributions from the major fluid components that drive variations in Earth's rotation. In this study, we use the AAM, OAM, HAM, and SLAM products provided by the GFZ [37]. Specifically, AAM represents the angular momentum generated by large-scale atmospheric motion and, from a physical standpoint, reflects atmospheric rotation and circulation patterns. Its variability is closely linked to factors such as atmospheric mass redistribution, wind speed, and angular-momentum exchange with the solid Earth. OAM arises from ocean dynamics, including large-scale circulation and various wave processes, and constitutes a significant component of the Earth system's angular momentum budget. HAM results from the transport, cycling, and redistribution of water within the hydrological cycle, encompassing contributions from rivers, lakes, groundwater, glaciers, snow cover, and soil moisture. SLAM is primarily associated with variations in sea level and surface-layer ocean dynamics, driven by processes such as sea-level changes, ocean circulation adjustments, and surface wave activity. All components are taken from the daily forecast products of the Earth System Modelling Group at the German Research Centre for Geosciences (ESMGFZ) data center, with the historical record starting on 1 January 2020. Since October 2024, GFZ has extended the forecast length of AAM, OAM, and related products from the original 6 days to 10 days. To ensure consistency throughout the study period, we uniformly adopt EAM forecasts with a maximum horizon of 10 days. Specifically, for each forecast initialization day m, we retrieve the 10-day ahead forecasts of AAM, OAM, HAM, and SLAM, and obtain the total EAM series by summing the four components on a day-by-day basis, as shown in Equation (1).

$$\mathrm{EAM} = \mathrm{AAM} + \mathrm{OAM} + \mathrm{HAM} + \mathrm{SLAM} \tag{1}$$

For short-term PM forecasts with lead times of 1 to m days, the EAM forecast values are utilized directly, while the residual between geodetic angular momentum (GAM) and EAM—termed the GAM residual—is extrapolated. Estimating the GAM residual is a key step in short-term PM prediction, and this requires first deriving GAM. The Liouville equations describe the differential relationship between PM and the angular momentum functions, as expressed in Equation (2).

$$p(t) + i\sigma_c \frac{\mathrm{d}p(t)}{\mathrm{d}t} = \chi(t) \tag{2}$$

Here, t denotes time, and PM is represented as $p(t) = p_X(t) - ip_Y(t)$, where $p_X(t)$ is the X component with its positive direction pointing toward the prime meridian, and $p_Y(t)$ is the Y component with its positive direction pointing toward 90°W. EAM is expressed as $\chi(t) = \chi_X(t) + i\chi_Y(t)$, where $\chi_X(t)$ and $\chi_Y(t)$ are the X and Y components used in multiparameter PM prediction based on EAM. In this formulation, the positive direction of $\chi_X(t)$ points toward the prime meridian, whereas the positive direction of $\chi_Y(t)$ points toward 90°E. Consequently, the minus sign preceding $p_Y(t)$ in the expression for $p(t)$ reflects the inconsistency between the adopted positive directions for PM and EAM [38].

σ_c denotes the complex Chandler frequency, given by $\sigma_c = 2\pi[1 + i/(2Q)]/T_{\mathrm{cw}}$. In this study, the Chandler wobble period is set to $T_{\mathrm{cw}} = 433$ days, and the quality factor is taken as $Q = 170$ [25–27]. A discrete form of the Liouville equations was further derived by Wilson as shown below [38–40]:

$$\chi(t) = \frac{i}{2\sigma_c \Delta t} \exp\left(-i\pi \frac{\Delta t}{T_{\mathrm{cw}}}\right)[p(t+\Delta t) + (1 - \exp(i\sigma_c \Delta t))p(t) - \exp(i\sigma_c \Delta t)p(t-\Delta t)] \tag{3}$$

$$p(t) = -i\sigma_c \Delta t \, 2 \exp\left(i\pi \frac{\Delta t}{T_{\mathrm{cw}}}\right)[\chi(t) + \chi(t - \Delta t)] + \exp(i\sigma_c \Delta t) p(t - \Delta t) \quad (4)$$

In Equations (3) and (4), Δt denotes the time increment. Since both PM and EAM datasets are provided as discrete time series, the discretized Liouville equations enable the transformation between PM and EAM [39,40]. As a result, GAM can be derived directly from the PM series via the Liouville equations. Using the transformation relationship between the EAM and PM described above, along with these datasets, the GAM and EAM series over the most recent four years are obtained, as illustrated in Figure 1.

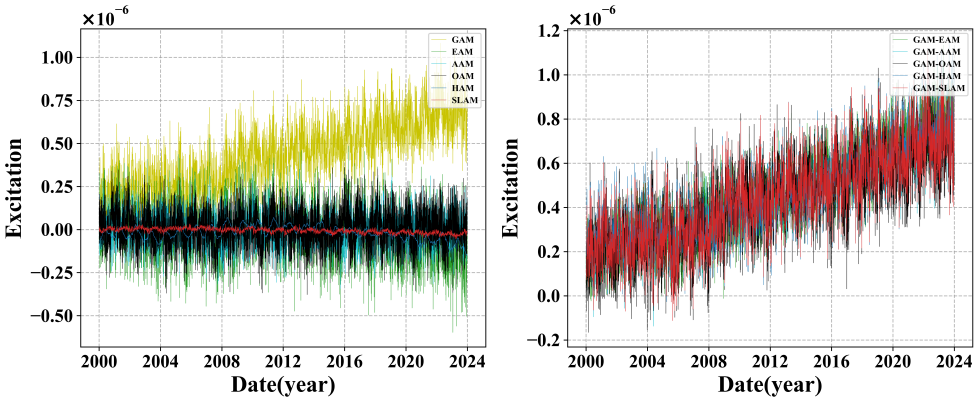

Figure 1. Time series of the χ_X components (2020–2024) and their differences with GAM.

As shown in Figures 1 and 2, the left panels display the time series of GAM, EAM, AAM, OAM, HAM, and SLAM over the period 2020–2024. The solid yellow curve represents the GAM series derived from IERS C04 PM X and Y data via the Liouville equations. The solid green curve denotes the total EAM series, while the solid light-blue, purple, blue, and red curves correspond to AAM, OAM, HAM, and SLAM, respectively. The right panels illustrate the differences between the GAM series and each of the EAM, AAM, OAM, HAM, and SLAM components. All series are dimensionless and plotted along the vertical axis.

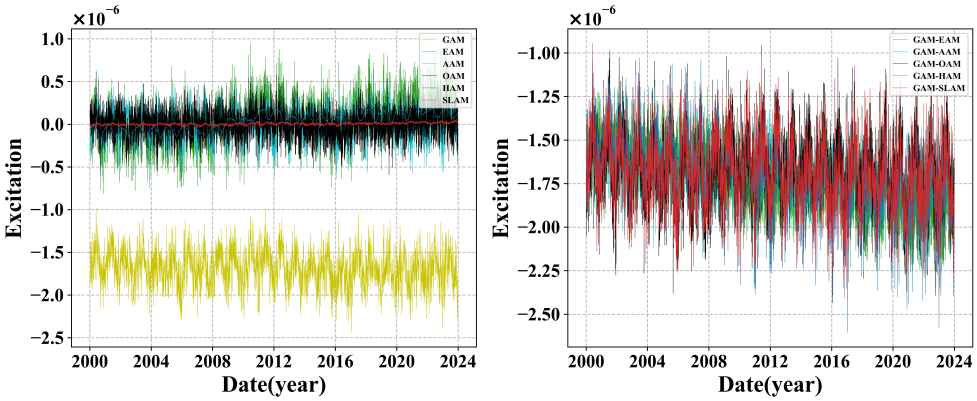

Figure 2. Time series of the χ_Y components (2020–2024) and their differences with GAM.

As shown in Figures 3 and 4, the periodic components of the GAM, EAM, AAM, OAM, HAM, and SLAM time series along the χ_X and χ_Y directions are presented, respectively. In the left panels, the yellow, green, light-blue, purple, blue, and red dashed curves represent the Fourier spectra of GAM, EAM, AAM, OAM, HAM, and SLAM, while the right panels show the corresponding sub-monthly Fourier spectra.

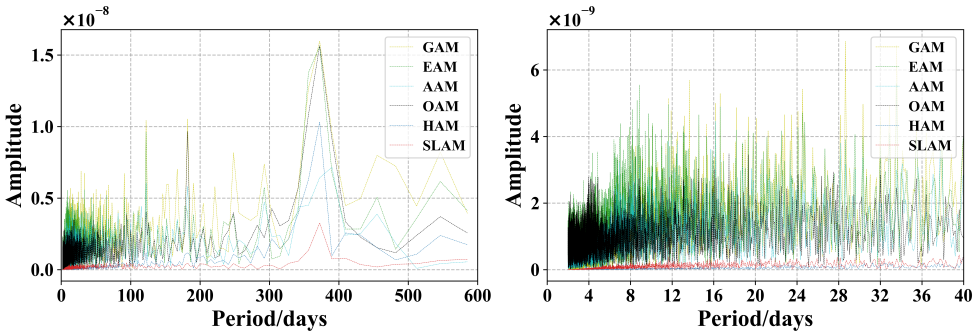

Figure 3. Periodic components of the χ_X series for each dataset.

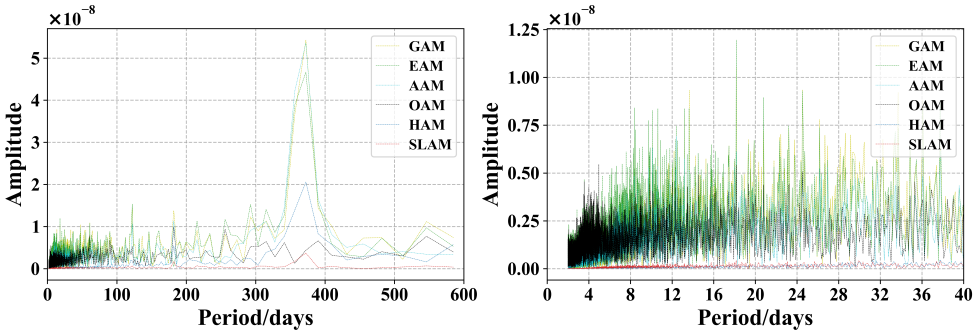

Figure 4. Periodic components of the χ_Y series for each dataset.

2.2. Analysis of EAM Forecast Accuracy

2.2.1. Prediction Error Metrics

For error assessment, the mean absolute error (MAE) is used as the primary metric for evaluating prediction accuracy and is defined in Equation (5).

$$\mathrm{MAE} = \frac{1}{N}\sum_{i=1}^{N}|f_i - o_i| \tag{5}$$

where f_i and o_i denote the forecast value and the corresponding reference value, respectively, and N denotes the sample size. The MAE directly quantifies the average magnitude of deviations between forecasts and reference values, thereby enabling a quantitative comparison of prediction accuracy across different methods.

2.2.2. Forecast Accuracy of the AAM/OAM/HAM/SLAM Datasets

This section evaluates the forecast accuracy of the χ_X and χ_Y components of the AAM, OAM, HAM, and SLAM datasets released by GFZ over the period from 1 January to 28 December 2024, with a particular focus on lead times ranging from 1 to 10 days. AAM represents the angular momentum generated by large-scale atmospheric motion and, from a physical perspective, reflects atmospheric rotation and circulation patterns. Its variability is closely associated with factors such as atmospheric mass redistribution, wind speed, and angular-momentum exchange with the solid Earth. OAM arises from oceanic dynamics, including large-scale circulation and various wave processes, and constitutes an important component of the Earth's angular momentum budget. HAM results from the transport, cycling, and redistribution of water within the hydrological cycle, encompassing contributions from rivers, lakes, groundwater, glaciers, snow cover, and soil moisture. SLAM is primarily associated with variations in sea-level and surface-layer ocean dynamics, driven by processes such as sea-level fluctuations, ocean circulation adjustments, and surface wave activity. The mass term refers to the contribution caused by mass redistribution, which modifies the inertia tensor of the Earth system. The motion term denotes the contribution

from the relative angular momentum associated with geophysical fluid motion, such as atmospheric winds, ocean currents, and hydrological transport.

Figures 5–9 summarize the forecast accuracy of the AAM, OAM, HAM, and SLAM products based on approximately 360 forecast results during 2024. The x-axis represents forecast lead time (1 to 10 days), and the y-axis shows the MAE. The native temporal resolution of the AAM and OAM products is 3 h, corresponding to about eight samples per day. As lead time increases, forecast errors generally grow due to sensitivity to initial conditions and the accumulation of high-frequency variability. In addition, the error evolution differs between mass and motion terms: mass terms tend to increase more smoothly and exhibit a near-monotonic trend, whereas motion terms are more prone to oscillatory behavior and stage-dependent changes in slope. This contrast is evident for both the X and Y components.

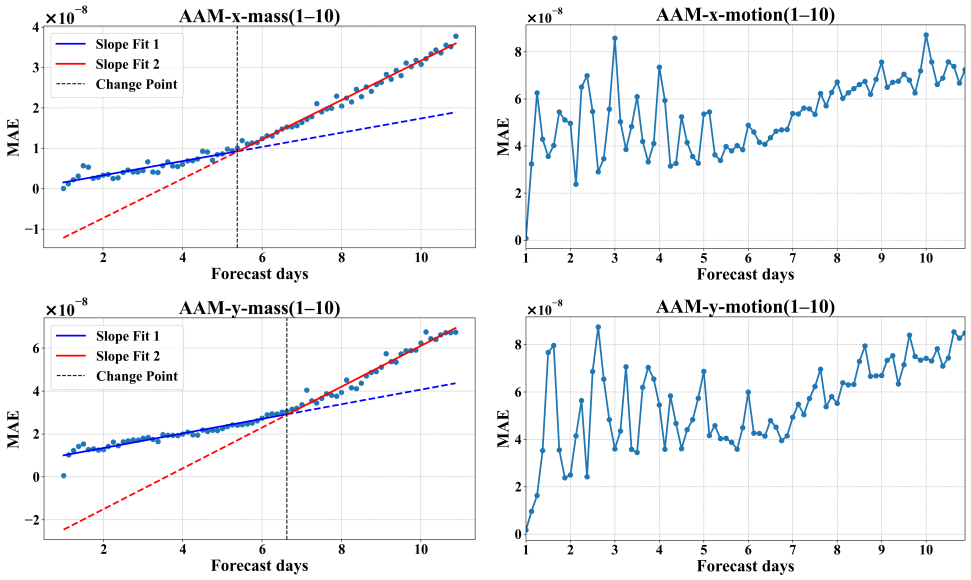

Figure 5. Forecast accuracy of AAM X and Y components during 2024 based on over 350 forecast results.

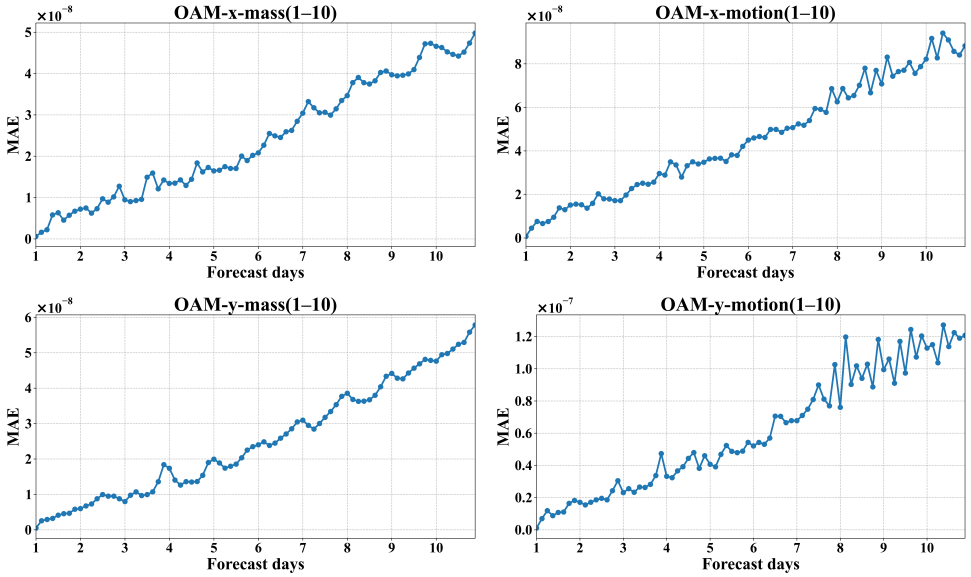

Figure 6. Forecast accuracy of OAM X and Y components during 2024 based on over 350 forecast results.

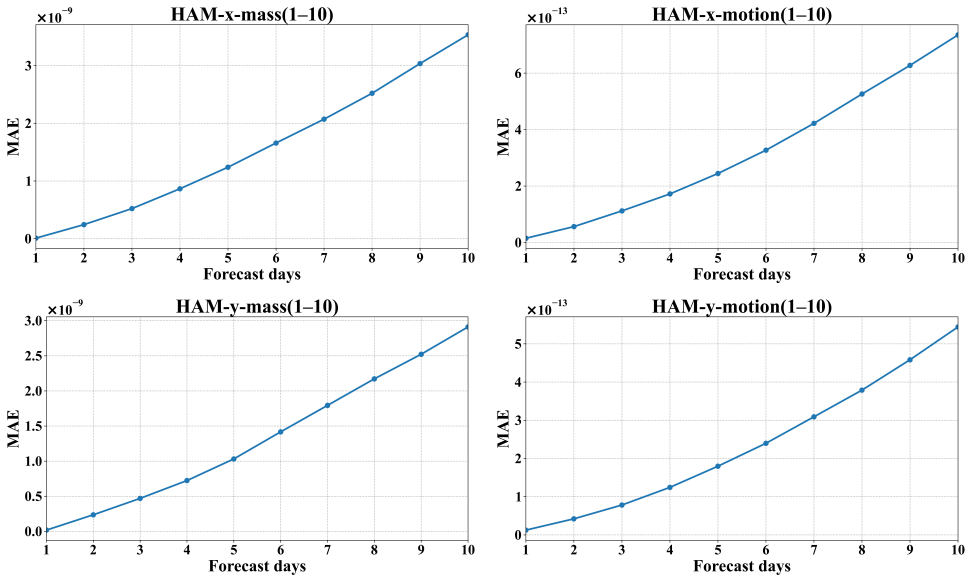

Figure 7. Forecast accuracy of HAM X and Y components during 2024 based on over 350 forecast results.

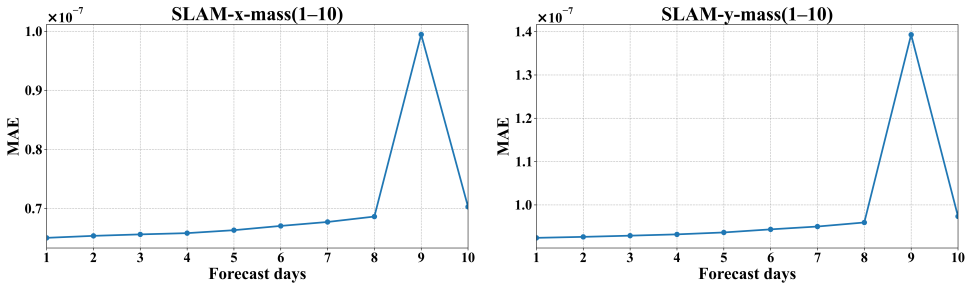

Figure 8. Forecast accuracy of SLAM X and Y components during 2024 based on over 350 forecast results.

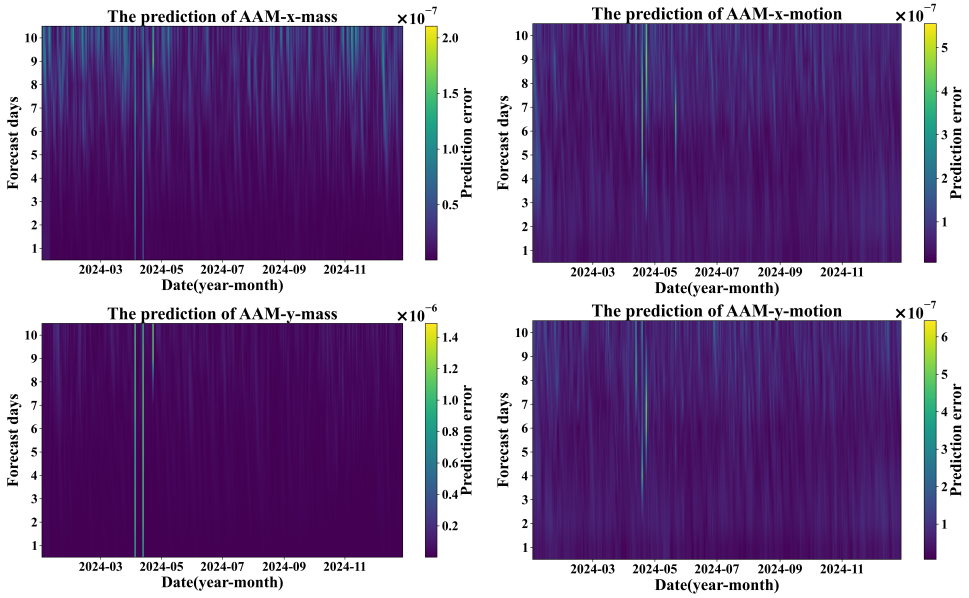

Figure 9. AAM forecast errors (1–10-day lead times) during 2024.

Figure 5 presents the statistical forecast accuracy for the X and Y components of AAM. The upper-left and lower-left panels correspond to the AAM-X mass term and AAM-Y mass term, respectively, showing how the MAE evolves with lead time, along with a piecewise linear slope fit. In each panel, the solid blue line represents the fitted slope for

the first segment, the solid red line represents the fitted slope for the second segment, and the vertical black dashed line indicates the change point. The plotted points and fitted curves show that the mass-term errors for both X and Y increase slowly during the early stage (approximately 1 to 7 days), resulting in a relatively flat trend. After the change point, error growth accelerates, and the fitted slope in the latter segment becomes notably steeper than in the former segment. This behavior suggests that short-term AAM mass-term forecasts are primarily influenced by relatively smooth, low-frequency variability. Beyond the mid-range, however, error accumulation becomes increasingly dominated by nonlinear perturbations, intraseasonal variability, and rapid processes that the model cannot fully capture.

The upper-right and lower-right panels of Figure 5 (AAM-X-motion and AAM-Y-motion) display the errors associated with the motion term. Over lead times of 1 to 5 days, the motion term exhibits pronounced saw-tooth-like fluctuations, with MAE varying considerably between consecutive lead days. This indicates that short-term errors are strongly influenced by high-frequency dynamical processes and transient signals—such as rapid AAM variations and synoptic-scale disturbances—for which the model provides less stable fits, resulting in notable variability in the MAE statistics. Beyond approximately days 5 to 6, both motion–term curves show a general upward trend. Although fluctuations persist, the error evolution is no longer characterized by purely irregular jumps; instead, MAE increases progressively with lead time and remains at a relatively elevated level. This transition—from strong early-stage oscillations to a sustained increase in the mid-to-late range—suggests that once a mid-range threshold is exceeded, the dominant source of model error shifts from discrete weather-related effects to systematic accumulation, accompanied by a notable reduction in predictability.

As shown in Figure 6, the statistical forecast accuracy for the X and Y components of OAM is summarized. The upper-left and lower-left panels (OAM-X-mass and OAM-Y-mass) display monotonically increasing MAE curves: the error rises rapidly from day 1 before entering a quasi-stationary growth regime, after which it increases steadily with forecast lead time, accompanied by only minor fluctuations. This behavior indicates that the error structure of the OAM mass term is relatively stable, characterized by gradual, lead-time-dependent accumulation. A comparison between the X and Y mass terms reveals that the Y-mass curve is consistently slightly higher than its X counterpart, and this difference becomes more pronounced in the mid-to-late range (approximately 6–10 days). This suggests that the OAM mass term in the Y direction contains, in a statistical sense, a larger unpredictable component; for instance, the superposition of low-frequency processes associated with oceanic mass redistribution may lead to greater error amplification at intermediate lead times.

In the upper-right and lower-right panels (OAM-X-motion and OAM-Y-motion), the motion-term behavior differs markedly between the two directions. The MAE of X-motion increases continuously and exhibits noticeable fluctuations near the long-lead end (around 8–10 days), while maintaining an overall coherent growth trajectory. In contrast, the Y-motion MAE reaches the 10^{-7} level—substantially higher than in the other three panels—and displays more frequent and sharper oscillations and spikes after approximately day 7. This indicates that the OAM motion term in the Y direction suffers from larger and more unstable errors at medium to long lead times. The higher error magnitude and stronger late-stage oscillations suggest that the Y-direction motion term encompasses more rapid variability and more complex coupling processes. Additionally, model errors for this component are more susceptible to isolated anomalous episodes, which can inflate the MAE and produce amplified jitter in the later forecast range.

Taken together with Figures 5 and 6, the mass terms in both X and Y are generally smoother, whereas the motion terms are more prone to strong oscillations and error intensification beyond a mid-range threshold. Specifically, the AAM mass term exhibits a distinct change point in slope around 5–7 days, while the OAM Y-motion component is characterized by a higher error level (10^{-7}) and more pronounced late-stage oscillations.

As shown in Figures 7 and 8, the HAM X and Y components exhibit a relatively stable, near-linear increase in error with forecast lead time. For the mass terms (HAM-X-mass and HAM-Y-mass), the MAE is on the order of 10^{-9} and accumulates steadily as lead time increases, indicating a stable error-growth pattern and a relatively small error magnitude for HAM mass-term forecasts. The motion terms (HAM-X-motion and HAM-Y-motion) show an even smaller error level, on the order of 10^{-13}, and also display approximately linear growth, suggesting that the model achieves high predictive accuracy for the HAM motion terms.

In contrast, the mass terms of SLAM for both X and Y (SLAM-X-mass and SLAM-Y-mass) exhibit an abrupt jump around day 9, with the error magnitude reaching the level 10^{-7}. This behavior points to notable instability in the SLAM mass-term MAE over the 8–10-day range, where anomalous data likely cause a sudden increase in forecast errors. This issue is further supported by the prediction-error heatmap analysis presented in the following section.

As shown in Figures 9 and 10, the statistics are presented without removing anomalous forecast outliers. The forecast errors of the AAM motion terms are substantially larger than those of the mass terms. This contrast aligns with the historical dominance of the wind-driven (motion) contribution in AAM variability, where the variance of the motion component is markedly greater than that of the pressure-driven (mass) component. The order of magnitude differences in the corresponding time series amplitudes make this behavior evident and confirm that motion-term errors are significantly larger than mass-term errors. Physically, atmospheric circulation processes—such as jet streams and tropical winds—constitute the primary drivers of AAM fluctuations. In addition, pronounced anomalous jumps are observed in the forecast datasets of AAM and SLAM on 4, 12, 18 and 22 April 2024, as well as on 21 May 2024. No comparable data anomalies are found in the OAM and HAM forecast datasets; therefore, these two components are not examined in further detail here.

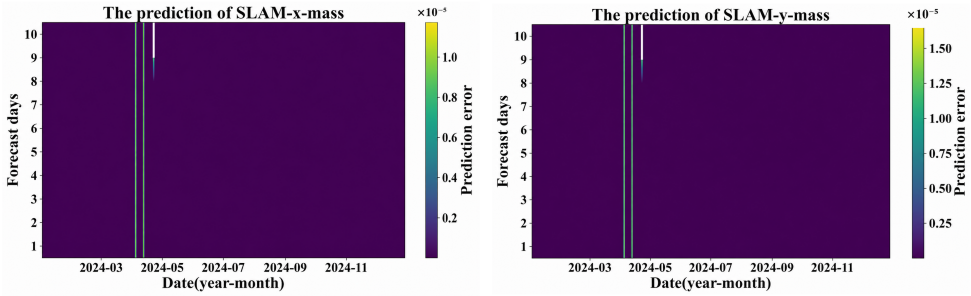

Figure 10. SLAM forecast errors (1–10-day lead times) during 2024.

Tables 1 and 2 report the MAE values for the AAM, OAM, HAM, and SLAM datasets along the χ_1 and χ_2 components, respectively. In the tables, the following abbreviations are used: AAM_ma denotes AAM mass term, AAM_mo denotes AAM motion term, OAM_ma denotes OAM mass term, OAM_mo denotes OAM motion term, HAM_ma denotes HAM mass term, HAM_mo denotes HAM motion term, and SLAM_ma denotes SLAM mass term. The MAE values in Table 1 are on the order of 10^{-8}, while those in Table 2 are uniformly on the order of 10^{-7}.

Table 1. MAE values for the AAM, OAM, HAM, and SLAM χ_X components.

MAE	AAM_ma	AAM_mo	HAM_ma	HAM_mo	OAM_ma	OAM_mo	SLAM_ma
1	0.288739	3.998977	0.000878	0.000001	0.419083	0.791937	6.503015
2	0.363825	4.776659	0.024322	0.000006	0.871636	1.646812	6.536651
3	0.536814	5.001532	0.052116	0.000011	1.181847	2.209247	6.561560
4	0.764874	4.486588	0.086505	0.000017	1.504802	3.215335	6.582526
5	1.046331	4.179842	0.123855	0.000024	1.797830	3.720858	6.632468
6	1.419876	4.508798	0.165814	0.000033	2.488366	4.778668	6.704911
7	1.927886	5.685745	0.207137	0.000042	3.141843	5.670949	6.771656
8	2.337194	6.476802	0.252066	0.000053	3.823793	6.910142	6.863274
9	2.902121	6.850444	0.303577	0.000063	4.224723	7.708150	9.946071
10	3.411432	7.329158	0.353441	0.000074	4.616599	8.744986	7.028787

Table 2. MAE values for the AAM, OAM, HAM, and SLAM χ_Y components.

MAE	AAM_ma	AAM_mo	HAM_ma	HAM_mo	OAM_ma	OAM_mo	SLAM_ma
1	0.113917	0.348159	0.000176	0	0.035519	0.106266	0.923939
2	0.15687	0.521004	0.002357	0	0.083238	0.201339	0.926196
3	0.185349	0.522549	0.004692	0.000001	0.113557	0.292478	0.928969
4	0.207973	0.476518	0.007231	0.000001	0.149032	0.397189	0.931971
5	0.243443	0.445467	0.01031	0.000002	0.198913	0.473413	0.936385
6	0.299233	0.450607	0.014162	0.000002	0.26138	0.614695	0.943525
7	0.369326	0.569378	0.017932	0.000003	0.321416	0.806627	0.950058
8	0.444525	0.663735	0.021713	0.000004	0.383084	0.989858	0.959387
9	0.562519	0.728503	0.025214	0.000005	0.453045	1.07882	1.392919
10	0.658406	0.779569	0.029104	0.000005	0.521165	1.168505	0.973471

2.3. Forecasting Method

The EAM + LS + AR Model for PM Prediction

In this study, PM is predicted using the EAM + LS + AR approach proposed by Dill et al. [20]. In the first stage, for lead times of 1 to m days—where m denotes the forecast horizon covered by the EAM dataset—an LS + AR model is applied to extrapolate the residual, which is then combined with the EAM forecast to generate EAM predictions for the next m days. These EAM predictions are subsequently converted into PM forecasts via the Liouville equations. In the second stage, the short-term EAM predictions for days 1–m are concatenated with the historical GAM series, and the extended series is extrapolated using LS + AR out to day 90 to produce EAM forecasts for lead times from m to 90 days. These forecasts are again transformed into PM predictions for days m–90 using the Liouville equations.

$$\chi_t = a_0 + a_1 t + a_2 t^2 + a_3 t^3 + a_4 t^4 + a_5 t^5 + a_6 t^6 + a_7 t^7 + \sum_{j=1}^{n} \left[b_j \sin\left(\frac{2\pi t}{T_j} + \phi_j\right) + b_j^* \cos\left(\frac{2\pi t}{T_j} + \phi_j^*\right) \right] \quad (6)$$

The LS fitting model is expressed in Equation (6), where a_0 through a_7 denote the parameters of the linear trend terms, and b_j, b_j^*, ϕ_j, and ϕ_j^* represent the coefficients of the periodic terms. The periods are set to $T_0 = 1$ year, $T_1 = 1/2$ year, $T_2 = 1/3$ year, and $T_3 = 13.7$ days [25,26]. An autoregressive model of order p, denoted as AR(p), is employed as given in Equation (7).

$$e_t = \phi_1 e_{t-1} + \cdots + \phi_p e_{t-p} + \omega_t \quad (7)$$

The AR coefficients, denoted ϕ_i, are parameters of the autoregressive model, where $\omega(t)$ represents white noise. The optimal lag order p for the model is determined using the

Akaike information criterion (AIC) [41]. After estimating the coefficients from the historical residuals, they are used to recursively generate forecasted residuals for the subsequent 90 days, resulting in the series $\widehat{e_{AR}}(t)$.

3. Impact of Different EAM Forecast Horizons on PM Prediction Accuracy

3.1. PM X Error Variations Across Forecast Lead Time and EAM Horizon

Using the EAM + LS + AR approach, we conducted over 350 PM X prediction experiments for the period from January to December 2024, with EAM forecast horizons ranging from 1 to 10 days. The detailed results are presented in Figure 11. The x-axis represents the forecast lead time in days, and the y-axis shows the MAE in milliarcseconds (mas). As indicated in the legend, the curves labeled 1 to 10 correspond to the MAE of PM X forecasts obtained using EAM forecast data of 1 to 10 days, respectively.

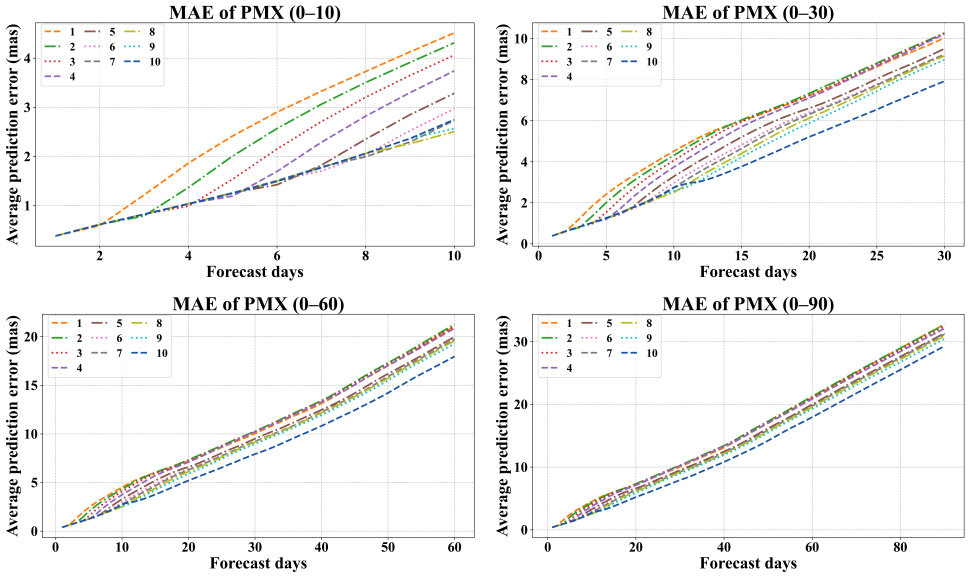

Figure 11. Prediction accuracy of the PM X component across different EAM forecast horizons.

As shown in Figure 11 and Table 3, the MAE difference at a forecast lead time of 10 days reaches 2.00865 mas when comparing the schemes using 1-day and 8-day EAM forecasts. At the 90th day, this difference attains its maximum value of 3.47429 mas between the 1-day and 10-day EAM forecast schemes. The prediction accuracy of PM X exhibits a systematic dependence on the length of the EAM forecast horizon. Specifically, for 1–2-day X forecasts, the highest accuracy is achieved using a 1-day EAM forecast. For a 3-day X forecast, the 2-day EAM horizon yields the best performance; for a 4-day forecast, the 3-day horizon is optimal; for a 5-day forecast, the 4-day horizon; for a 6-day forecast, the 5-day horizon; for a 7-day forecast, the 6-day horizon; and for an 8-day forecast, the 7-day horizon provides the highest accuracy. For 9–10-day X forecasts, the best performance is obtained with an 8-day EAM horizon. For medium- to long-range forecasts (12–90 days), using a 10-day EAM horizon consistently yields the lowest MAE and thus the best overall accuracy. Across all schemes, errors increase with forecast lead time, which naturally reflects the accumulation of forecast uncertainty.

Table 3. PM X prediction accuracy (MAE) across different EAM forecast horizons.

MAE	1	2	3	4	5	6	7	8	9	10
1 days	0.38186	0.38186	0.38186	0.38186	0.38186	0.38186	0.38186	0.38107	0.38107	0.38107
2 days	0.59153	0.61708	0.61708	0.61708	0.61708	0.61708	0.61708	0.61474	0.61474	0.61474
3 days	1.21566	0.78731	0.82423	0.82423	0.82423	0.82423	0.82423	0.82106	0.82106	0.82106
4 days	1.86250	1.36741	0.98824	1.03821	1.03821	1.03821	1.03821	1.03302	1.03302	1.03302
5 days	2.41666	2.00797	1.53654	1.19338	1.25963	1.25963	1.25963	1.24997	1.24997	1.24997
6 days	2.89996	2.56758	2.15058	1.69390	1.42374	1.50871	1.50871	1.49306	1.49306	1.49306
7 days	3.32698	3.06130	2.70827	2.28645	1.82088	1.70305	1.78882	1.77032	1.77032	1.77032
8 days	3.72874	3.50426	3.20375	2.81975	2.35080	2.03170	1.99343	2.06093	2.06093	2.06093
9 days	4.12822	3.91280	3.64762	3.29714	2.84791	2.52314	2.29414	2.25893	2.36315	2.36315
10 days	4.51338	4.31206	4.06165	3.74102	3.28440	2.97168	2.73239	2.50473	2.56652	2.74991
15 days	6.00599	6.03399	5.94080	5.70128	5.20002	4.81986	4.64164	4.39750	4.21994	3.76432
20 days	7.22044	7.32647	7.22527	7.10065	6.60302	6.40061	6.30678	6.12292	5.87927	5.20944
25 days	8.62061	8.80064	8.74104	8.67524	8.03739	7.77367	7.73849	7.62463	7.44008	6.54259
30 days	10.03573	10.27638	10.24947	10.21716	9.50558	9.20876	9.22723	9.15148	8.96709	7.92607
35 days	11.59171	11.86459	11.80572	11.70571	10.93405	10.57550	10.62109	10.56131	10.40975	9.31868
40 days	13.13009	13.42057	13.35888	13.28227	12.47804	12.09831	12.24449	12.15921	11.93521	10.81945
45 days	15.05666	15.35203	15.19757	15.04748	14.18597	13.77807	13.93578	13.83762	13.60031	12.45157
50 days	17.01094	17.30644	17.17729	17.03687	16.18535	15.78333	15.90875	15.74462	15.49863	14.21902
55 days	19.03107	19.26943	19.09286	18.90711	18.04199	17.67442	17.82059	17.67356	17.44531	16.16154
60 days	21.06875	21.26764	21.07678	20.86419	19.99384	19.61947	19.75474	19.57693	19.28270	17.96556
65 days	23.09817	23.25332	23.04958	22.81071	21.95035	21.59558	21.72369	21.52218	21.18582	19.86489
70 days	25.08348	25.19372	24.97813	24.71438	23.86875	23.53695	23.65411	23.43528	23.05869	21.76839
75 days	27.03464	27.09917	26.87262	26.58488	25.75870	25.45246	25.55827	25.32305	24.92212	23.65742
80 days	28.94974	28.96828	28.73217	28.42236	27.61997	27.34060	27.43459	27.17278	26.75006	25.51930
85 days	30.88142	30.85360	30.60899	30.27859	29.50423	29.25265	29.33370	29.05256	28.60963	27.41840
90 days	32.76335	32.68928	32.43730	32.08769	31.34552	31.12398	31.19222	30.89542	30.43477	29.28906

3.2. PM Y Error Variations Across Forecast Lead Time and EAM Horizon

As shown in Figure 12, over 350 PM Y prediction experiments were conducted for the period from January to December 2024 using the EAM + LS + AR approach, with EAM forecast horizons ranging from 1 to 10 days. The x-axis represents the forecast lead time in days, and the y-axis shows the MAE in mas. As indicated in the legend, the curves labeled 1 to 10 correspond to the MAE of PM Y forecasts obtained using EAM forecast data of 1 to 10 days, respectively.

As shown in Figure 12 and Table 4, the influence of the EAM forecast horizon on the prediction accuracy of PM Y is more nuanced than that observed for PM X. The lower-right panel of Figure 12 indicates that, at a lead time of 43 days, the maximum MAE difference among the various EAM horizons reaches 2.00475 mas (between the 1-day and 10-day EAM schemes). As the lead time extends further, this maximum difference tends to decrease gradually, dropping to just 0.39513 mas by day 90. After approximately 80 days, the MAE curves for different EAM horizons begin to converge noticeably, suggesting that for Y forecasts at lead times of 80 days and beyond, prediction accuracy becomes largely independent of the chosen EAM horizon length.

At a lead time of 10 days, the MAE difference is 2.02586 mas (between the 1-day and 9-day EAM schemes), and this difference peaks at day 25, reaching 2.27183 mas (between the 1-day and 10-day EAM schemes). Overall, the prediction accuracy of PM Y exhibits a systematic dependence on the length of the EAM horizon. For short-range Y forecasts (1–9 days), the highest accuracy is achieved using an 8-day EAM forecast. For the 10-day PM Y forecast, the 9-day EAM horizon yields the best performance. For medium- to long-range forecasts (11–90 days), the scheme employing a 10-day EAM horizon consistently achieves the lowest MAE and therefore the best accuracy. Similar to the pattern observed

for PM X, the errors across all schemes increase with forecast lead time, which reflects the expected accumulation of forecast uncertainty. However, the rate of increase and the magnitude of the errors vary considerably depending on the EAM horizon used.

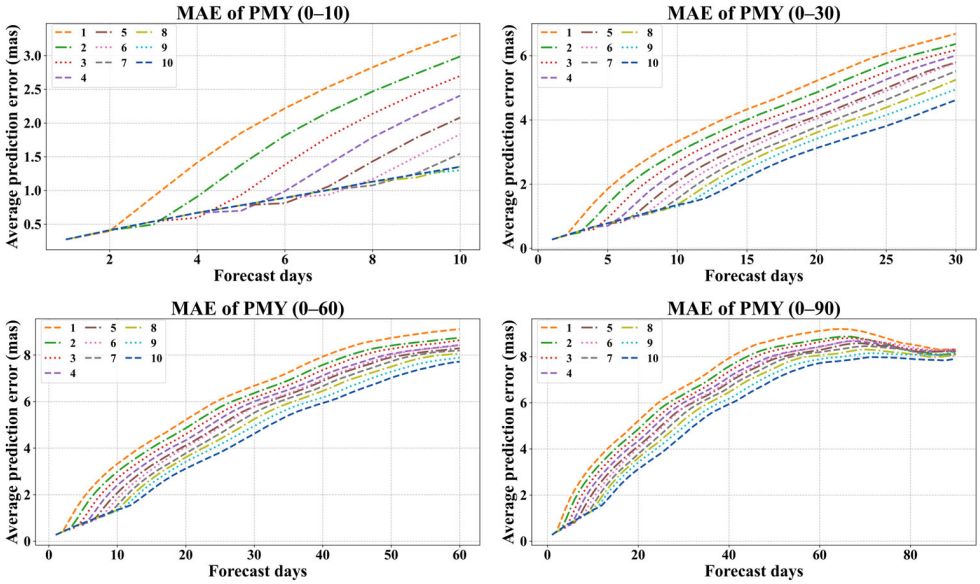

Figure 12. Prediction accuracy of the PM Y component across different EAM forecast horizons.

Table 4. PM Y prediction accuracy (MAE) across different EAM forecast horizons.

MAE	1	2	3	4	5	6	7	8	9	10
1 days	0.27475	0.27475	0.27475	0.27475	0.27475	0.27475	0.27475	0.27469	0.27469	0.27469
2 days	0.39920	0.41066	0.41066	0.41066	0.41066	0.41066	0.41066	0.41177	0.41177	0.41177
3 days	0.91052	0.49525	0.54134	0.54134	0.54134	0.54134	0.54134	0.54114	0.54114	0.54114
4 days	1.41567	0.90948	0.59622	0.66952	0.66952	0.66952	0.66952	0.67028	0.67028	0.67028
5 days	1.85304	1.38024	0.93493	0.69950	0.78024	0.78024	0.78024	0.78146	0.78146	0.78146
6 days	2.21843	1.81401	1.38190	0.99007	0.81216	0.89097	0.89097	0.89273	0.89273	0.89273
7 days	2.53778	2.16482	1.79877	1.39222	1.06113	0.93744	1.00819	1.00820	1.00820	1.00820
8 days	2.82651	2.46772	2.13722	1.78778	1.43065	1.16647	1.07621	1.13147	1.13147	1.13147
9 days	3.09385	2.73212	2.43705	2.11381	1.78198	1.50190	1.25267	1.19321	1.23885	1.23885
10 days	3.32505	2.98706	2.69755	2.40591	2.08092	1.83392	1.54540	1.35461	1.29919	1.35254
15 days	4.32931	4.00817	3.76502	3.50840	3.26022	3.07997	2.87439	2.67290	2.47635	2.21023
20 days	5.21771	4.85607	4.60168	4.33760	4.11614	4.04276	3.78076	3.60722	3.41355	3.12369
25 days	6.08052	5.76123	5.50259	5.26056	4.98746	4.90462	4.62800	4.38903	4.15000	3.80869
30 days	6.68231	6.36482	6.17448	6.00421	5.78958	5.78197	5.52158	5.25058	4.94942	4.61907
35 days	7.25460	6.91308	6.70844	6.50944	6.29620	6.35244	6.13804	5.92894	5.68795	5.40751
40 days	7.93116	7.57588	7.35848	7.11582	6.88745	6.95098	6.66149	6.45812	6.17446	5.93629
45 days	8.44680	8.09548	7.90770	7.63711	7.44126	7.50852	7.23912	7.03910	6.75962	6.48340
50 days	8.73542	8.40600	8.25897	8.04987	7.90093	7.99168	7.72646	7.49953	7.28239	7.01934
55 days	8.94918	8.58203	8.45335	8.26730	8.13879	8.25671	8.05991	7.90349	7.67922	7.43649
60 days	9.11395	8.74093	8.63597	8.43330	8.28800	8.41127	8.19325	8.05705	7.88519	7.71596
65 days	9.19229	8.86580	8.79229	8.63268	8.50430	8.61377	8.33318	8.16648	7.99774	7.82671
70 days	9.06208	8.76380	8.74052	8.63041	8.55933	8.71882	8.45165	8.30573	8.13405	7.95171
75 days	8.78022	8.52075	8.56219	8.47656	8.43444	8.60100	8.37779	8.21802	8.11534	7.96548
80 days	8.53688	8.26940	8.33134	8.26829	8.23981	8.41958	8.24513	8.10647	8.08946	7.90410
85 days	8.34581	8.12793	8.23710	8.22632	8.20934	8.28604	8.07475	7.97997	8.07084	7.85709
90 days	8.30894	8.15409	8.32849	8.26862	8.23621	8.31805	8.10630	8.05428	8.22104	7.91381

From the temporal evolution of forecast errors across different EAM schemes, the following observations can be made. (1) In the short-term range (1–10 days), prediction

error decreases monotonically as the EAM horizon lengthens: a 1-day horizon is insufficient to capture the full spectrum of short-term excitation, resulting in relatively large errors, whereas horizons of 9–10 days largely encompass the dominant high-frequency excitation and thus produce the smallest errors. (2) In the medium- to long-term range (12–90 days), EAM horizons of 9 days or longer consistently outperform shorter-horizon schemes, with only a marginal difference in performance between the 9-day and 10-day options. These findings indicate that, for both the PM X and Y components, the effective saturation horizon is approximately 9–10 days; using a 10-day EAM forecast yields performance comparable to that of a 9-day forecast, while horizons shorter than 9 days result in a progressive degradation of medium- to long-range prediction accuracy.

4. Discussion

4.1. Segmented PM X/Y Prediction with Varying EAM Forecast Horizons and Resulting Accuracy

The analyses presented in Sections 3.1 and 3.2 demonstrate that the choice of EAM forecast horizon exerts a pronounced influence on the prediction of PM X/Y. For PM X, the maximum MAE difference attains 3.47429 mas, while for PM Y, it reaches 2.00475 mas. Motivated by these findings, we develop a lead-time–adaptive PM X/Y prediction system. Within the EAM + LS + AR forecasting framework, this system assigns a specific EAM forecast horizon to each individual lead time, thereby maximizing the prediction accuracy of PM X/Y through a tailored horizon selection strategy.

The lead-time-dependent horizon selection pattern was first identified using the 2020–2023 development period. For each year in this period, PM X and PM Y predictions were generated using EAM forecast horizons from 1 to 10 days, and the mean absolute error (MAE) was computed for each prediction lead time and horizon. The development period results show a consistent lead-time-dependent pattern. For 1–10-day forecasts, the optimal horizon follows a consistent systematic rule for both PM X and Y: a forecast at day m attains the highest accuracy when an EAM horizon of $m - 1$ days is used. For long-range forecasts of PM X and Y, a 10-day EAM horizon provides the best overall performance.

The 2024 rolling prediction experiments were then used as an independent evaluation to test whether this development period pattern remained valid. As summarized in Table 5, the optimal horizons obtained from the 2024 evaluation are broadly consistent with the development period pattern. These results indicate that the segmented EAM horizon strategy is not solely tuned to the 2024 evaluation year, but reflects a pattern already observed in the 2020–2023 development period.

Table 5. Optimal EAM forecast horizons for PMX and PMY prediction obtained from the independent 2024 evaluation.

Forecast Days	EAM of PMX	Forecast Days	EAM of PMY
1–2	1	1–2	1
3	2	3	2
4	3	4	3
5	4	5	4
6	5	6	5
7	6	7	6
8	7	8	7
9–10	8	9	8
11	9	10	9
12–90	10	11–90	10

Table 5 presents the optimal EAM forecast horizons for PM X/Y prediction. For lead times of 1 to 10 days, the optimal horizons for both components follow a consistent pattern:

a forecast at day m achieves the highest accuracy when an EAM horizon of m-1 days is employed. For long-range PM X/Y prediction, a 10-day EAM forecast horizon yields the best overall performance.

4.2. Comparison with the IERS Method

For comparative evaluation, we use the daily PM forecasts provided by the IERS Rapid Service/Prediction Center as a reference. These forecasts extend to 90 days, and the full 90-day predictions are adopted for the comparison in this study. Since the IERS forecasts themselves already incorporate some AAM information (e.g., Bulletin A applies NCEP atmospheric forecasts to correct short-term PM variations), this comparison offers a meaningful benchmark for quantifying the improvement of the proposed method relative to existing operational forecasts.

4.2.1. Comparison of PM X Predictions with IERS Rapid Products

As shown in Figure 13 and Table 6, the MAE of PM X forecasts obtained with different EAM forecast horizons is compared against that of the IERS rapid product. Based on full-year experimental statistics from 2024 using the EAM + LS + AR framework, all EAM horizon configurations yield improvements over the entire lead-time range (1–90 days), albeit to varying degrees. Across the ten experiments, a total of 900 MAE data points are obtained, of which 83.5% outperform the IERS rapid product.

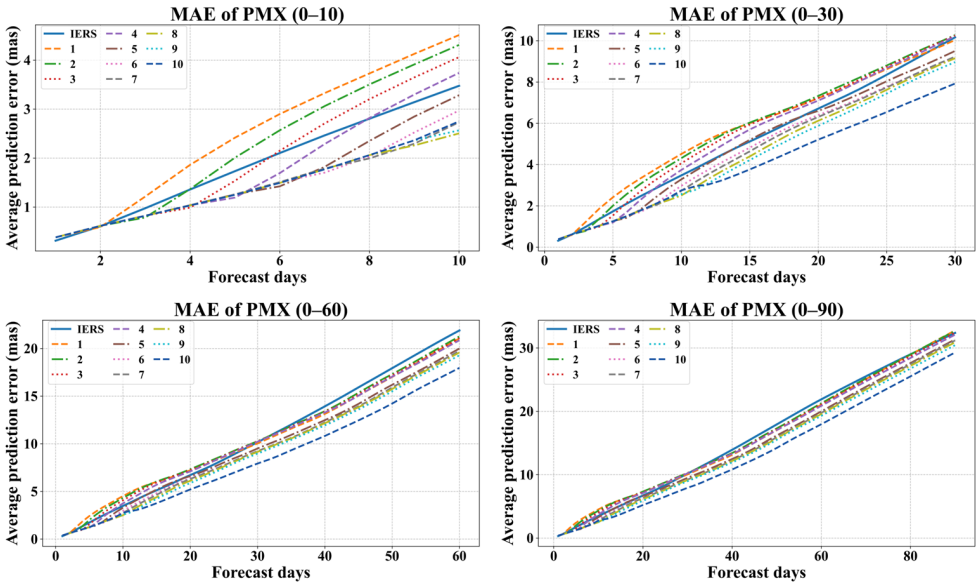

Figure 13. Comparison of MAE for PM X forecasts using different EAM horizons and the IERS rapid product.

For PM X, using a 1-day EAM horizon results in 58.89% of lead times exhibiting better accuracy than the IERS rapid product; the corresponding proportions are 55.56% for a 2-day horizon, 66.67% for a 3-day horizon, 72.22% for a 4-day horizon, and 92.22% for a 5-day horizon. When the EAM horizon is extended to 6–10 days, 97.78% of lead times achieve higher accuracy than the IERS rapid product. For medium-range forecasts (30–75 days), all schemes with EAM horizons from 1 to 10 days outperform the IERS rapid product, with positive MAE reduction observed throughout this interval. The influence of the EAM horizon on the MAE of PM X is also substantial: for instance, at a 15-day lead time, adopting a 10-day EAM horizon improves prediction accuracy by 43.79% relative to the 1-day EAM scheme. These results indicate that the EAM forecast horizon is a critical

factor in PM X prediction, and employing horizon-dependent segmented forecasting yields marked improvements across short-, medium-, and long-range predictions.

Table 6. MAE reduction in PM X forecasts using different EAM horizons relative to the IERS daily product.

MAE	1	2	3	4	5	6	7	8	9	10
1	−21.73%	−21.73%	−21.73%	−21.73%	−21.73%	−21.73%	−21.73%	−21.48%	−21.48%	−21.48%
2	2.93%	−1.27%	−1.27%	−1.27%	−1.27%	−1.27%	−1.27%	−0.88%	−0.88%	−0.88%
3	−24.51%	19.36%	15.58%	15.58%	15.58%	15.58%	15.58%	15.91%	15.91%	15.91%
4	−37.06%	−0.62%	27.28%	23.60%	23.60%	23.60%	23.60%	23.98%	23.98%	23.98%
5	−39.46%	−15.88%	11.33%	31.13%	27.31%	27.31%	27.31%	27.87%	27.87%	27.87%
6	−37.87%	−22.07%	−2.24%	19.47%	32.31%	28.27%	28.27%	29.02%	29.02%	29.02%
7	−35.08%	−24.29%	−9.96%	7.17%	26.07%	30.86%	27.37%	28.13%	28.13%	28.13%
8	−32.96%	−24.96%	−14.24%	−0.55%	16.17%	27.55%	28.92%	26.51%	26.51%	26.51%
9	−31.39%	−24.53%	−16.09%	−4.94%	9.36%	19.70%	26.99%	28.11%	24.79%	24.79%
10	−29.83%	−24.04%	−16.84%	−7.62%	5.52%	14.52%	21.40%	27.95%	26.17%	20.89%
15	−17.33%	−17.87%	−16.05%	−11.37%	−1.58%	5.84%	9.33%	14.09%	17.56%	26.46%
20	−7.59%	−9.17%	−7.66%	−5.80%	1.61%	4.63%	6.03%	8.77%	12.40%	22.38%
25	−3.23%	−5.39%	−4.68%	−3.89%	3.75%	6.91%	7.33%	8.69%	10.90%	21.65%
30	1.28%	−1.09%	−0.82%	−0.51%	6.49%	9.41%	9.23%	9.98%	11.79%	22.03%
35	3.49%	1.21%	1.70%	2.54%	8.96%	11.95%	11.57%	12.07%	13.33%	22.41%
40	5.72%	3.64%	4.08%	4.63%	10.40%	13.13%	12.08%	12.69%	14.30%	22.31%
45	5.41%	3.56%	4.53%	5.47%	10.88%	13.44%	12.45%	13.07%	14.56%	21.78%
50	5.13%	3.48%	4.20%	4.98%	9.73%	11.97%	11.27%	12.19%	13.56%	20.70%
55	4.58%	3.39%	4.27%	5.20%	9.54%	11.38%	10.65%	11.39%	12.53%	18.97%
60	3.76%	2.85%	3.72%	4.69%	8.67%	10.38%	9.76%	10.57%	11.92%	17.94%
65	2.63%	1.98%	2.84%	3.84%	7.47%	8.97%	8.43%	9.28%	10.69%	16.26%
70	1.72%	1.28%	2.13%	3.16%	6.48%	7.78%	7.32%	8.17%	9.65%	14.71%
75	0.90%	0.66%	1.49%	2.55%	5.58%	6.70%	6.31%	7.17%	8.64%	13.28%
80	0.16%	0.10%	0.91%	1.98%	4.75%	5.71%	5.39%	6.29%	7.75%	11.99%
85	−0.58%	−0.49%	0.31%	1.38%	3.90%	4.72%	4.46%	5.38%	6.82%	10.70%
90	−1.19%	−0.96%	−0.18%	0.90%	3.19%	3.87%	3.66%	4.58%	6.00%	9.54%

4.2.2. Comparison of PM Y Predictions with IERS Rapid Products

As shown in Figure 14 and Table 7, the MAE of PM Y forecasts obtained with different EAM forecast horizons is compared against that of the IERS rapid product. Based on full-year experimental statistics from 2024 using the EAM + LS + AR framework, varying the EAM horizon yields improvements over the IERS rapid product to varying extents, primarily in short-term PM Y forecasts. For PM Y, using EAM horizons of 1–6 days results in only 2% to 10% of lead times achieving higher accuracy than the IERS rapid product. These proportions increase to 12.22% for a 7-day horizon, 14.44% for an 8-day horizon, 17.78% for a 9-day horizon, and 28.89% for a 10-day horizon.

Compared with the substantial MAE reductions observed for PM X under varying EAM horizons, the impact on PM Y is largely concentrated in the short-range predictions (1–15 days), where differences among forecasts obtained with different horizons can reach approximately 2 mas. For example, at a 9-day lead time, adopting a 10-day EAM horizon improves prediction accuracy by a factor of two relative to the 1-day EAM scheme; compared with the IERS rapid product, accuracy improves by 34.62%. These results indicate that the EAM forecast horizon is a critical factor for short-term PM Y prediction, and that horizon-dependent segmented forecasting can yield substantial improvements in the short range.

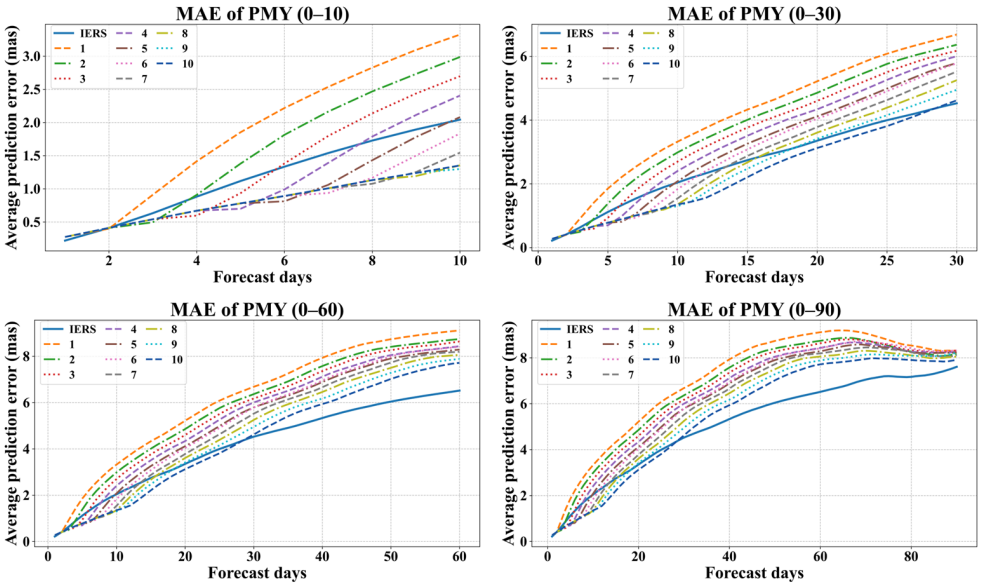

Figure 14. Comparison of MAE for PM Y forecasts using different EAM horizons and the IERS rapid product.

Table 7. MAE reduction in PM Y forecasts using different EAM horizons relative to the IERS daily product.

MAE	1	2	3	4	5	6	7	8	9	10
1	−24.96%	−24.96%	−24.96%	−24.96%	−24.96%	−24.96%	−24.96%	−24.93%	−24.93%	−24.93%
2	2.61%	−0.19%	−0.19%	−0.19%	−0.19%	−0.19%	−0.19%	−0.46%	−0.46%	−0.46%
3	−43.79%	21.79%	14.51%	14.51%	14.51%	14.51%	14.51%	14.54%	14.54%	14.54%
4	−60.43%	−3.06%	32.44%	24.13%	24.13%	24.13%	24.13%	24.04%	24.04%	24.04%
5	−65.74%	−23.45%	16.38%	37.43%	30.21%	30.21%	30.21%	30.10%	30.10%	30.10%
6	−66.30%	−35.98%	−3.59%	25.78%	39.12%	33.21%	33.21%	33.08%	33.08%	33.08%
7	−64.83%	−40.60%	−16.83%	9.58%	31.08%	39.11%	34.52%	34.52%	34.52%	34.52%
8	−63.63%	−42.86%	−23.72%	−3.49%	17.18%	32.47%	37.70%	34.50%	34.50%	34.50%
9	−63.28%	−44.19%	−28.61%	−11.56%	5.96%	20.74%	33.89%	37.03%	34.62%	34.62%
10	−62.76%	−46.21%	−32.04%	−17.77%	−1.86%	10.23%	24.36%	33.69%	36.41%	33.80%
11	−61.34%	−46.50%	−34.24%	−20.86%	−7.80%	2.90%	14.93%	25.38%	33.54%	34.31%
12	−61.07%	−46.99%	−36.00%	−23.86%	−12.11%	−3.18%	7.09%	16.98%	25.67%	33.16%
13	−60.43%	−46.77%	−36.57%	−25.81%	−15.13%	−6.66%	1.80%	10.97%	18.64%	28.59%
14	−58.87%	−46.44%	−36.82%	−26.77%	−17.06%	−9.95%	−1.93%	6.06%	13.43%	23.97%
15	−57.78%	−46.08%	−37.21%	−27.86%	−18.82%	−12.25%	−4.76%	2.59%	9.75%	19.45%

4.3. Component-Dependent Improvement and Robustness of the Segmented Strategy

The improvement achieved by the segmented strategy differs between PM X and PM Y. For PM X, the benefit of selecting appropriate EAM horizons is observed over a relatively broad lead-time range. For PM Y, however, the improvement is mainly concentrated in the short term, and the MAE curves corresponding to different EAM horizons gradually converge at longer lead times. This suggests that PM Y is more sensitive to short-term excitation accuracy, while its long-range prediction error is less dependent on the specific EAM forecast horizon.

Several anomalous AAM and SLAM forecast cases were observed in 2024. These anomalous values may affect the absolute MAE statistics for some initialization dates, especially in the short-term range. However, the segmented horizon selection strategy proposed in this study is derived from the overall behavior of a large number of rolling prediction experiments rather than from individual anomalous cases. Therefore, the main

lead-time-dependent pattern is not expected to be dominated by a few abnormal EAM forecasts. Nevertheless, robust outlier detection, EAM denoising, and sensitivity experiments excluding anomalous initialization dates will be considered in future work to further improve the stability of PM prediction.

4.4. Future Perspectives on Climate Regime Dependence and Advanced Forecasting Architectures

ENSO-related atmospheric and oceanic variability may influence EAM forecast errors and PM prediction performance. Future work will investigate whether the lead-time-dependent EAM horizon rule remains stable under different climate backgrounds, such as El Niño, La Niña, and neutral conditions.

The proposed segmented EAM horizon strategy is complementary to recent nonlinear and deep-learning-based PM prediction methods. LSTM-, EEMD-LSTM-, and transformer-based models mainly improve the statistical or nonlinear prediction backbone, whereas the present study focuses on the selection of the physical excitation input window. Therefore, the segmented EAM horizon strategy could potentially be combined with more advanced forecasting architectures in future work.

5. Conclusions

This study systematically investigated PM X and Y prediction using the EAM + LS + AR approach, with a particular focus on how the length of the EAM forecast horizon affects prediction accuracy. Building on these analyses, we proposed a segmented PM forecasting framework that improves full-range prediction accuracy for PM X and enhances short-term accuracy for PM Y (1–15 days) by adopting horizon-specific optimal EAM settings. The main conclusions are summarized as follows:

(a) Adjusting the EAM forecast horizon can significantly reduce prediction errors for PM X and Y. Using segmented PM prediction with varying EAM horizons improves short- to medium-range accuracy for PM X by 20–30% (1–60 days) relative to the IERS rapid product, and enhances long-range accuracy by 10–20% (61–90 days). For PM Y, short-term accuracy is improved by 20–40% (1–15 days) compared with the IERS rapid product.

(b) The influence of the EAM forecast horizon on long-range prediction accuracy for PM Y gradually diminishes. In the 70–90-day range, error differences among long-horizon schemes fall below 2 mas. At a 90-day lead time, the errors of all schemes essentially converge to approximately 8 mas.

(c) A segmented optimization framework for PM prediction is proposed, in which different EAM horizons are selected for different lead-time ranges. For 1–10-day forecasts, the optimal horizon follows a consistent systematic rule for both PM X and Y: a forecast at day m attains the highest accuracy when an EAM horizon of $m - 1$ days is used. For long-range forecasts of PM X and Y, a 10-day EAM horizon provides the best overall performance.

(d) The proposed approach demonstrates clear advantages over the official IERS forecasts. With the segmented strategy, PM X predictions outperform the IERS daily product across the entire 1–90-day range, while PM Y predictions surpass the daily forecasts issued by the IERS Rapid Service in the short term. In the 2024 test, 83.5% of PM X forecasts (1–90 days) and 50.78% of PM Y forecasts (1–15 days) exhibited smaller errors than the IERS daily product.

Overall, this study demonstrates that the EAM forecast horizon has a substantial impact on PM prediction accuracy, and that appropriate selection and utilization of EAM forecasts can effectively enhance forecasting performance. The proposed segmented optimization framework improves the PM forecasting procedure by increasing prediction accuracy.

Future work may incorporate EAM denoising and integrate additional techniques—such as filtering, assimilation, and machine-learning-based forecasting—to further advance PM prediction skill.

Author Contributions: Material preparation, data collection, and analysis were performed by Y.C. and X.L. Implementation and validation of the prediction algorithms were conducted by Y.C. and X.L. The first draft of the manuscript was written by Y.C., Y.W. and X.L. provided comments on the experimental design and data analysis of the first draft. H.Q. and Y.W. commented on the discussion section of the previous version of the manuscript and reviewed the full text. D.Y., Z.Z. (Zewen Zhang), Z.Z. (Zhizhuo Zhang), and X.Y. contributed to data checking, result verification, and manuscript review. All authors have read and agreed to the published version of the manuscript.

Funding: This study was funded by the Strategic Priority Research Program of the Chinese Academy of Sciences (Grant No. XDB1070202, XDB1070301, XDB1070302). H-H.Q. was supported by Youth Innovation Promotion Association, CAS.

Data Availability Statement: The IERS C04 can be downloaded at: http://hpiers.obspm.fr/iers/eop/eopc04_14/eopc04_IAU2000.62-now (accessed on 26 March 2026), the finals.daily can be downloaded at: https://datacenter.iers.org/products/eop/rapid/daily/finals2000A.daily (accessed on 26 March 2026), the Bulletin A can be downloaded at: https://datacenter.iers.org/products/eop/rapid/bulletina (accessed on 26 March 2026), and the EOP predictions of the 2nd EOP PCC can be downloaded at: https://doi.org/10.5880/GFZ.1.3.2023.001 (accessed on 26 March 2026).

Acknowledgments: The IERS C04 series, the Bulletin A series, the finals.daily series, and the forecast data from the 2nd EOP PCC were used in this study. We express our gratitude to the respective data providers for making these resources available.

Conflicts of Interest: The authors declare no conflicts of interest.

Abbreviations

The following abbreviations are used in this manuscript:

PM	Polar motion
PMX	X component of polar motion
PMY	Y component of polar motion
EOP	Earth orientation parameter
ERP	Earth rotation parameter
EAM	Effective angular momentum
AAM	Atmospheric angular momentum
OAM	Oceanic angular momentum
HAM	Hydrological angular momentum
SLAM	Sea-level angular momentum
GAM	Geodetic angular momentum
LS	Least squares
AR	Autoregressive model
AIC	Akaike information criterion
LOD	Length of day
UT1	Universal Time 1
UTC	Coordinated Universal Time
IERS	International Earth Rotation and Reference Systems Service
GFZ	German Research Centre for Geosciences
VLBI	Very Long Baseline Interferometry
GNSS	Global Navigation Satellite System
SLR	Satellite Laser Ranging

References

1. Dill, R.; Dobslaw, H.; Thomas, M. Combination of modeled short-term angular momentum function forecasts from atmosphere, ocean, and hydrology with 90-day EOP predictions. *J. Geod.* **2013**, *87*, 567–577. [CrossRef]
2. Li, C.; Li, X.; Wu, Y.; Yang, X.; Qiao, H.; Yang, H. Improved LOD and UT1-UTC Prediction Using Least Squares Combined with Polynomial CURVE Fitting. *Remote Sens.* **2024**, *16*, 4393. [CrossRef]
3. Bizouard, C.; Lambert, S.; Gattano, C.; Becker, O.; Richard, J.Y. The IERS EOP 14C04 solution for Earth orientation parameters consistent with ITRF 2014. *J. Geod.* **2018**, *93*, 621–633. [CrossRef]
4. Gambis, D. Monitoring Earth orientation using space-geodetic techniques: State-of-the-art and prospective. *J. Geod.* **2004**, *78*, 295–303. [CrossRef]
5. Artz, T.; Bernhard, L.; Nothnagel, A.; Steigenberger, P.; Tesmer, S. Methodology for the combination of sub-daily Earth rotation from GPS and VLBI observations. *J. Geod.* **2011**, *86*, 221–239. [CrossRef]
6. Nastula, J.; Chin, T.M.; Gross, R.; Śliwińska, J.; Wińska, M. Smoothing and predicting celestial pole offsets using a Kalman filter and smoother. *J. Geod.* **2020**, *94*, 29. [CrossRef]
7. Gambis, D.; Luzum, B. Earth rotation monitoring, UT1 determination and prediction. *Metrologia* **2011**, *48*, S165–S170. [CrossRef]
8. Li, X.; Yang, X.; Ye, R.; Cheng, X.; Zhang, S. Research on Methods to Improve Length of Day Precision by Combining with Effective Angular Momentum. *Remote Sens.* **2024**, *16*, 722. [CrossRef]
9. Li, X.; Lou, J.; Yuan, Y.; Wu, J.; Zhang, K. Determination of global geodetic parameters using satellite laser ranging to Galileo, GLONASS, and BeiDou satellites. *Satell. Navig.* **2024**, *5*, 10. [CrossRef]
10. Kong, Q.; Han, J.; Wu, Y.; Wang, T.; Chen, Y. High-precision polar motion prediction using EOP_20_C04 and EAM based on CSLS+AR and CSLS+LSTM methods. *Geophys. J. Int.* **2023**, *235*, 1658–1670. [CrossRef]
11. Kehm, A.; Hellmers, H.; Bloßfeld, M.; Dill, R.; Angermann, D.; Seitz, F.; Hugentobler, U.; Dobslaw, H.; Thomas, M.; Thaller, D.; et al. Combination strategy for consistent final, rapid and predicted Earth rotation parameters. *J. Geod.* **2023**, *97*, 3. [CrossRef]
12. Li, X.; Wu, Y.; Yao, D.; Liu, J.; Nan, K.; Ma, L.; Cheng, X.; Yang, X.; Zhang, S. Research on UT1-UTC and LOD Prediction Algorithm Based on Denoised EAM Dataset. *Remote Sens.* **2023**, *15*, 4654. [CrossRef]
13. Guo, J.Y.; Li, Y.B.; Dai, C.L.; Shum, C.K. A technique to improve the accuracy of Earth orientation prediction algorithms based on least squares extrapolation. *J. Geodyn.* **2013**, *70*, 36–48. [CrossRef]
14. Wu, Y.; Zhao, X.; Yang, X. Improved Prediction of Polar Motions by Piecewise Parameterization. *Artif. Satell.* **2022**, *57*, 290–299. [CrossRef]
15. Akulenko, L.D.; Kumakshev, S.A.; Markov, Y.G.; Rykhlova, L.V. A Model for the polar motion of the deformable Earth adequate for astrometric data. *Astron. Rep.* **2002**, *46*, 74–82. [CrossRef]
16. Akulenko, L.D.; Kumakshev, S.A.; Markov, Y.G.; Rykhlova, L.V. Forecasting the polar motions of the deformable Earth. *Astron. Rep.* **2002**, *46*, 858–865. [CrossRef]
17. Schuh, H.; Ulrich, M.; Egger, D.; Müller, J.; Schwegmann, W. Prediction of Earth orientation parameters by artificial neural networks. *J. Geod.* **2002**, *76*, 247–258. [CrossRef]
18. Dill, R.; Saynisch-Wagner, J.; Irrgang, C.; Thomas, M. Improving Atmospheric Angular Momentum Forecasts by Machine Learning. *Earth Space Sci.* **2021**, *8*, e2021EA002070. [CrossRef]
19. Chao, B.F.; Chung, W.; Shih, Z.; Hsieh, Y. Earth's rotation variations: A wavelet analysis. *Terra Nova* **2014**, *26*, 260–264. [CrossRef]
20. Dill, R.; Dobslaw, H.; Thomas, M. Improved 90-day Earth orientation predictions from angular momentum forecasts of atmosphere, ocean, and terrestrial hydrosphere. *J. Geod.* **2018**, *93*, 287–295. [CrossRef]
21. Xu, X.Q.; Zhou, Y.H.; Liao, X.H. Short-term earth orientation parameters predictions by combination of the least-squares, AR model and Kalman filter. *J. Geodyn.* **2012**, *62*, 83–86. [CrossRef]
22. Xu, X.; Zhou, Y. EOP prediction using least square fitting and autoregressive filter over optimized data intervals. *Adv. Space Res.* **2015**, *56*, 2248–2253. [CrossRef]
23. Kalarus, M.; Schuh, H.; Kosek, W.; Akyilmaz, O.; Bizouard, C.; Gambis, D.; Gross, R.; Jovanović, B.; Kumakshev, S.; Kutterer, H.; et al. Achievements of the Earth orientation parameters prediction comparison campaign. *J. Geod.* **2010**, *84*, 587–596. [CrossRef]
24. Śliwińska Bronowicz, J.; Kur, T.; Wińska, M.; Dobslaw, H.; Nastula, J.; Partyka, A.; Belda, S.; Bizouard, C.; Boggs, D.; Bruni, S.; et al. Assessment of length-of-day and universal time predictions based on the results of the Second Earth Orientation Parameters Prediction Comparison Campaign. *J. Geod.* **2024**, *98*, 22. [CrossRef]
25. Brzeziński, A.; Nastula, J. Oceanic excitation of the chandler wobble. *Adv. Space Res.* **2002**, *30*, 195–200. [CrossRef]
26. Aoyama, Y.; Naito, I. Atmospheric excitation of the Chandler wobble, 1983–1998. *J. Geophys. Res. Solid Earth* **2001**, *106*, 8941–8954. [CrossRef]
27. Furuya, M.; Chao, B.F. Estimation of period and Q of the Chandler wobble. *Geophys. J. Int.* **1996**, *127*, 693–702. [CrossRef]
28. Dobslaw, H.; Dill, R. Predicting Earth orientation changes from global forecasts of atmosphere-hydrosphere dynamics. *Adv. Space Res.* **2018**, *61*, 1047–1054. [CrossRef]

29. Kouba, J. Comparison of polar motion with oceanic and atmospheric angular momentum time series for 2-day to Chandler periods. *J. Geod.* **2005**, *79*, 33–42. [CrossRef]
30. Ponte, R.M.; Ali, A.H. Rapid ocean signals in polar motion and length of day. *Geophys. Res. Lett.* **2002**, *29*, 6-1–6-4. [CrossRef]
31. Rekier, J.; Chao, B.F.; Chen, J.; Dehant, V.; Rosat, S.; Zhu, P. Earth's Rotation: Observations and Relation to Deep Interior. *Surv. Geophys.* **2021**, *43*, 149–175. [CrossRef]
32. Gross, R.S.; Fukumori, I.; Menemenlis, D.; Gegout, P. Atmospheric and oceanic excitation of length-of-day variations during 1980–2000. *J. Geophys. Res. Solid Earth* **2004**, *109*, B01406. [CrossRef]
33. Sabadini, R.; Riva, R.E.M.; Dalla Via, G. Coseismic rotation changes from the 2004 Sumatra earthquake: The effects of Earth's compressibility versus earthquake induced topography. *Geophys. J. Int.* **2007**, *171*, 231–243. [CrossRef]
34. Dill, R.; Stumpe, L.; Saynisch-Wagner, J.; Thomas, M.; Dobslaw, H. Benefits of refined 10-day effective angular momentum forecasts for earth rotation parameter prediction. *J. Geod.* **2025**, *99*, 15. [CrossRef]
35. Dill, R.; Dobslaw, H. Short-term polar motion forecasts from earth system modeling data. *J. Geod.* **2010**, *84*, 529–536. [CrossRef]
36. Dill, R.; Dobslaw, H.; Thomas, M. ESMGFZ EAM Products for EOP Prediction: Toward the Quantification of Time Variable EAM Forecast Errors. *Artif. Satell.* **2023**, *58*, 330–340. [CrossRef]
37. Dobslaw, H.; Dill, R.; Grötzsch, A.; Brzeziński, A.; Thomas, M. Seasonal polar motion excitation from numerical models of atmosphere, ocean, and continental hydrosphere. *J. Geophys. Res. Solid Earth* **2010**, *115*, B10406. [CrossRef]
38. Fang, M.; Hager, B.H.; Liao, X.; Zhou, Y.; Xu, X. Revisit the theory of Earth rotation—Anatomy of the Liouville equation. *Geophys. J. Int.* **2022**, *229*, 2175–2191. [CrossRef]
39. Luo, J.; Chen, W.; Ray, J.; Li, J. Short-Term Polar Motion Forecast Based on the Holt-Winters Algorithm and Angular Momenta of Global Surficial Geophysical Fluids. *Surv. Geophys.* **2022**, *43*, 1929–1945. [CrossRef]
40. Wilson, C.R. Discrete polar motion equations. *Geophys. J. Int.* **1985**, *80*, 551–554. [CrossRef]
41. Akaike, H. A new look at the statistical model identification. *IEEE Trans. Autom. Control* **1974**, *19*, 716–723. [CrossRef]

Disclaimer/Publisher's Note: The statements, opinions and data contained in all publications are solely those of the individual author(s) and contributor(s) and not of MDPI and/or the editor(s). MDPI and/or the editor(s) disclaim responsibility for any injury to people or property resulting from any ideas, methods, instructions or products referred to in the content.